An arithmetic rule for spatial summation of excitatory and inhibitory inputs in pyramidal neurons

Jiang Hao[a,1], Xu-dong Wang[a,1], Yang Dan[b], Mu-ming Poo[a,b,2], and Xiao-hui Zhang[a,2]

[a]Institute of Neuroscience and State Key Laboratory of Neuroscience, Shanghai Institutes for Biological Sciences, Chinese Academy of Sciences, 320 Yue-Yang Road, Shanghai 200031, China; and [b]Division of Neurobiology, Department of Molecular and Cell Biology, Helen Wills Neuroscience Institute, University of California, Berkeley, CA 94720

Contributed by Mu-ming Poo, November 3, 2009 (sent for review July 19, 2009)

Dendritic integration of excitatory and inhibitory inputs is critical for neuronal computation, but the underlying rules remain to be elucidated. Based on realistic modeling and experiments in rat hippocampal slices, we derived a simple arithmetic rule for spatial summation of concurrent excitatory glutamatergic inputs (*E*) and inhibitory GABAergic inputs (*I*). The somatic response can be well approximated as the sum of the excitatory postsynaptic potential (EPSP), the inhibitory postsynaptic potential (IPSP), and a nonlinear term proportional to their product (*kEPSP*IPSP), where the coefficient *k* reflects the strength of shunting effect. The *k* value shows a pronounced asymmetry in its dependence on *E* and *I* locations. For *I* on the dendritic trunk, *k* decays rapidly with *E–I* distance for proximal *E*s, but remains largely constant for distal *E*s, indicating a uniformly high shunting efficacy for all distal *E*s. For *I* on an oblique branch, the shunting effect is restricted mainly within the branch, with the same proximal/distal asymmetry. This asymmetry can be largely attributed to cable properties of the dendrite. Further modeling studies showed that this rule also applies to the integration of multiple coincident *E*s and *I*s. Thus, this arithmetic rule offers a simple analytical tool for studying *E–I* integration in pyramidal neurons that incorporates the location specificity of GABAergic shunting inhibition.**

dendrite integration | dendritic summation | neuronal computation | shunting inhibition | synaptic physiology

Neural information processing depends critically on the summation of excitatory postsynaptic potentials (EPSPs) and inhibitory postsynaptic potentials (IPSPs) at the dendrite, a process that determines the change in the somatic membrane potential and the pattern of neuronal spiking. Rall (1) proposed that the summation of EPSPs is sublinear for inputs at the same dendritic branch, but linear for those at different branches. Measurements in hippocampal CA1 pyramidal neurons (2) showed that the summation of EPSPs was indeed largely linear except at distal apical dendrites. Realistic modeling studies further yielded an arithmetic rule for dendritic integration of excitatory inputs; EPSPs are first integrated nonlinearly at individual branches before summed linearly at the soma (3, 4). This "two-layer network" model was supported by experiments using focal synaptic stimulation and glutamate uncaging (5, 6).

Although much is known about the summation of multiple EPSPs, it is unclear how EPSPs summate with IPSPs and whether there is a simple arithmetic rule applicable to excitatory glutamatergic input (*E*)–inhibitory GABAergic inputs (*I*) integration in a complex dendritic tree. A GABAergic input exerts two forms of inhibition: a hyperpolarization that is summed linearly with the depolarization (1, 7, 8) and a nonlinear reduction of the EPSP amplitude by shunting the depolarizing current through $GABA_A$ receptors ($GABA_A$Rs) (1, 8, 9). The nonlinear shunting effect has been commonly modeled as a divisive operation (8, 9), although some biophysical studies suggested that *E–I* summation may be more complex (10). The nonlinear shunting effect in *E–I* summation is known to depend on the dendritic location of synaptic inputs. Previous theoretical and modeling studies have shown that shunting inhibition is most effective when *I* is on the direct path from *E* to the soma ("on-the-path" theory; refs. 10 and 11). However, the dependence of shunting on the relative locations of *I* and *E* has not been systematically examined by experiment (but see ref. 12). Different types of inhibitory interneurons are known to selectively innervate distinct dendritic domains of pyramidal neurons in the hippocampus (13) and neocortex (14). Thus, quantitative characterization of the dendritic location dependence of nonlinear *E–I* integration is necessary for understanding the functional consequence of domain-specific inhibition.

Using iontophoretic application of glutamate and GABA in hippocampal slices and a realistic model of the CA1 pyramidal neuron, we have derived a simple arithmetic rule for predicting somatic responses to a pair of coactivated excitatory and inhibitory inputs. These responses could be well approximated by the sum of EPSP, IPSP, and a nonlinear component proportional to the product of EPSP and IPSP (*k**EPSP*IPSP). The dependence of the coefficient *k* on *E–I* locations provided direct support for the on-the-path theory. Furthermore, we found that shunting inhibition is uniform for all distal *E*s by a given *I*, but it decays rapidly with *E–I* distance for proximal *E*s. This arithmetic rule incorporates the location-specific features of *E–I* summation and provides a useful tool for quantitative analysis of dendritic integration.

Results

Experimental Measurements of *E–I* Integration. We first developed a quantitative assay of *E-I* integration in CA1 pyramidal neurons of rat hippocampal slices. The whole-cell recording was made from the soma of the pyramidal cell, and fluorescent dye Alexa Fluor 488 was loaded into the cell via the recording pipette to visualize the dendritic tree (Fig. 1*A*). Microiontophoretic applications of glutamate and GABA at the apical dendrite elicited rapid membrane depolarizations and hyperpolarizations with kinetics similar to those of natural EPSPs and IPSPs elicited by extracellular electrical stimulation in the CA1 region, respectively (Fig. 1*B* and *SI Appendix*). For convenience, these iontophoretic responses are referred to hereafter as EPSPs and IPSPs. When the EPSP and IPSP were elicited simultaneously with two iontophoretic pipettes placed at adjacent locations of the dendritic trunk, the measured somatic response was always smaller than the linear sum of the EPSP and IPSP measured separately (Fig. 1*B*). The nonlinear component of *E–I* integration was obtained by subtracting the measured sum from the linear sum. The amplitude of the nonlinear component was not affected by changing the driving force for the IPSP from −10 to 0 mV (Fig. S1 *C* and *D*) and was absent for summation of EPSP and hyperpolarization induced by somatic current injection

Author contributions: Y.D., M.-m.P., and X.-h.Z. designed research; J.H. and X.-d.W. performed research; J.H., X.-d.W., Y.D., M.-m.P., and X.-h.Z. analyzed data; and Y.D., M.-m.P., and X.-h.Z. wrote the paper.

The authors declare no conflict of interest.

[1]J.H. and X.-d.W. contributed equally to this work.

[2]To whom correspondence may be addressed. E-mail: mpoo@berkeley.edu or xhzhang@ion.ac.cn.

This article contains supporting information online at www.pnas.org/cgi/content/full/0912022106/DCSupplemental.

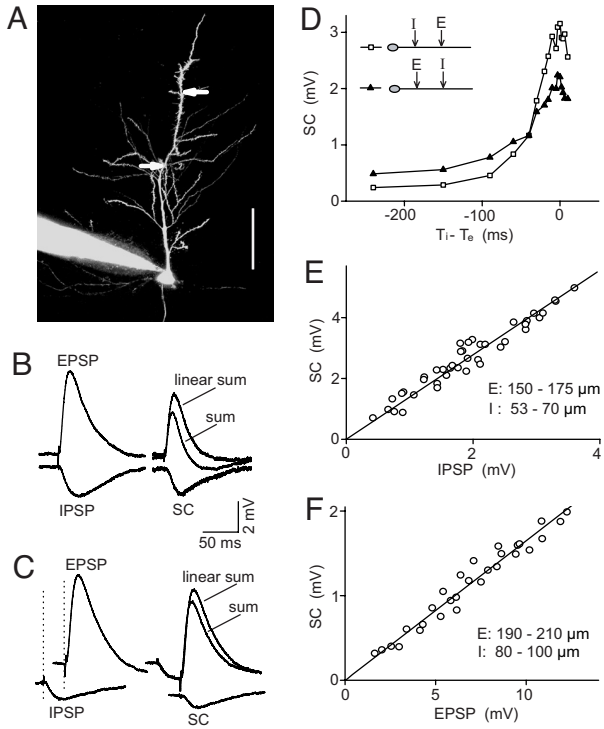

Fig. 1. Experimental measurement of *E–I* integration and its dependence on EPSP and IPSP amplitudes. (*A*) Image of a CA1 pyramidal neuron filled with Alexa Fluor 488 via the recording pipette. Arrows indicate pipettes for iontophoresis of glutamate and GABA (at 232 and 129 μm from soma). (Scale bar: 100 μm.) (*B*) Examples of EPSP, IPSP, their linear sum, and response to simultaneous glutamate and GABA pulses. SC is the recorded response (sum) minus the linear sum. (*C*) As in *B* except that IPSP preceded EPSP by 30 ms. (*D*) Changes in the amplitude of SC vs. the time interval between IPSP and EPSP, for two different sets of *E/I* location (square: *I* at 50–100 μm, *E* at 150–200 μm, $n = 6$; triangles: *E* at 100–150 μm, *I* at 200–250 μm, $n = 5$). (*E*) SC vs. IPSP amplitude, measured for a fixed EPSP amplitude (9–10 mV). Data are from four cells. Line indicares linear fit ($R = 0.974$). (*F*) SC vs. EPSP amplitude, measured for a fixed IPSP amplitude (1.1–1.3 mV). Data are from four cells. Line indicates linear fit ($R = 0.965$).

(Fig. S1 *E* and *F*), indicating that this nonlinear component reflects shunting inhibition. Thus, this nonlinear component was referred to as the shunting component (SC) (Fig. 1*B*).

We next examined how the temporal shift between *E* and *I* affects the amplitude of the SC, as illustrated by Fig. 1*C* for a case in which *I* preceded *E* for 30 ms. The SC amplitude decreased rapidly with the *E–I* interval, but significant shunting effect remained when *I* preceded *E* for up to 200 ms (Fig. 1*D*). Further pharmacological experiments indicated that prolonged inhibition with large *E–I* temporal intervals was mainly caused by the activation of $GABA_BRs$, because bath application of the $GABA_BR$ antagonist CGP 35348 (60 μM) abolished this prolonged component (Fig. S2). In the present study, we focused on the fast shunting inhibition for concurrent *E* and *I*, which is caused by opening of $GABA_ARs$.

To analyze *E–I* integration quantitatively, the amplitude of *E* was defined as the peak value of EPSP, whereas the amplitudes of *I* and the summed response were defined as the values at the time of the peak EPSP. Under this definition, we examined how the SC amplitude depends on the amplitude of EPSPs and IPSPs. By setting the EPSP amplitude at a fixed value while varying the IPSP amplitude, we found that the SC amplitude depended linearly on the IPSP amplitude (Fig. 1*E*). Conversely, at a fixed IPSP amplitude the SC amplitude depended linearly on the EPSP amplitude (Fig. 1*F*). Such linear dependence was also found if we define the amplitude by the mean EPSP/IPSP value over the first 100 ms (Fig. S3).

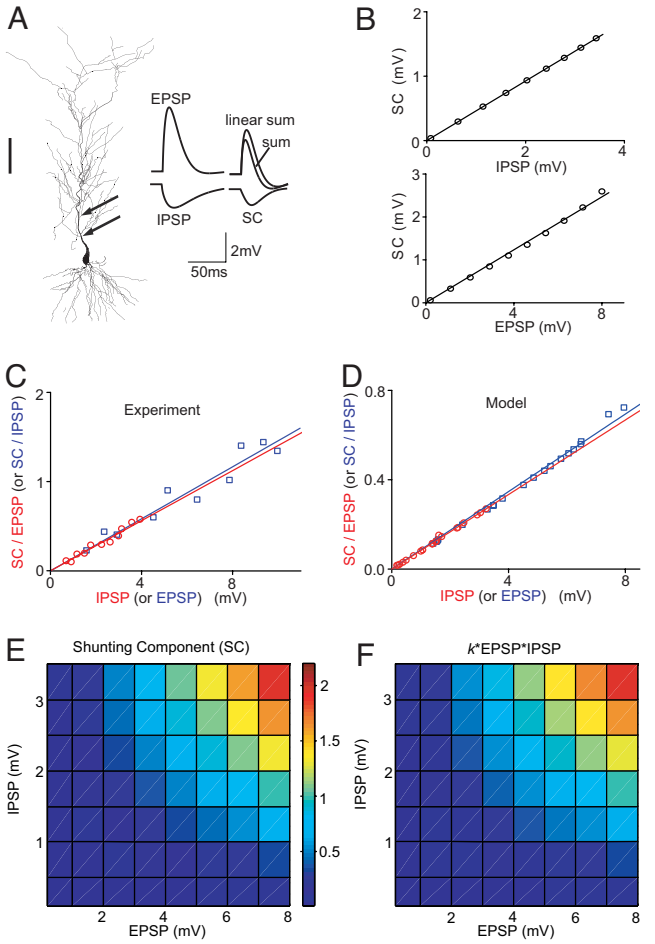

Fig. 2. Simulation of *E–I* integration in a realistic neuronal model and derivation of the arithmetic rule. (*A*) (*Left*) Reconstructed hippocampal CA1 pyramidal neuron used for simulation. Arrows indicate *I* and *E* were at 94 and 151 μm from the soma. (Scale: 100 μm.) (*Right*) Simulated EPSP, IPSP, their linear sum, simulated response (sum) of concurrently activated *E* and *I*, and the SC. (*B*) (*Upper*) SC vs. IPSP amplitude, with fixed EPSP amplitude (at 5.5 mV). Line indicates linear fit ($R = 0.999$). (*Lower*) SC vs. EPSP amplitude, with fixed IPSP amplitude (at 3.5 mV). Line indicates linear fit ($R = 0.998$). (*C*) Ratio between measured SC and EPSP (SC/EPSP) plotted against IPSP (red circle) and SC/IPSP plotted against EPSP (blue square) for the same cell in the slice recording. The amplitudes of the paired EPSP and IPSP were randomly set in the range of 1–10 and 0.2–4 mV, respectively. *E* and *I* locations were fixed at 110 and 45 μm. Lines indicate linear fit (red: $R = 0.96$, slope $k = 0.142$, $n = 11$; blue: $R = 0.92$, slope $k = 0.145$, $n = 10$). (*D*) Simulated SC/EPSP vs. IPSP (red circle, $n = 20$) and SC/IPSP vs. EPSP (blue square, $n = 20$). Lines indicate linear fit (red: $R = 0.999$, slope $k = 0.086$; blue: $R = 0.999$, slope $k = 0.087$). The EPSP amplitudes were randomly chosen from a 0.2- to 8-mV pool and the IPSP amplitude was from a 0.1- to 3.5-mV pool. *I* and *E* are at 94 and 151 μm. (*E*) Simulated SC as a function of both EPSP (0.2–8 mV) and IPSP (0.1–3.5 mV) amplitudes, with *E* and *I* at 202 and 123 μm, respectively. (*F*) k*EPSP*IPSP, with k adjusted to best fit the data in *E*; $k = 0.093$, rms error: 4.9%.

Derivation of Arithmetic Rule for *E–I* Integration by Modeling. To further investigate the shunting inhibition, we performed computer simulation with a realistic neuron model, using the morphology of a reconstructed CA1 pyramidal cell (15) (Fig. 2*A*) and the kinetics and distributions of ion channels reported previously (*SI Appendix*). The model parameters were adjusted to yield EPSPs and IPSPs (Fig. 2*A*) with kinetics similar to the experimentally observed iontophoretic EPSPs and IPSPs (Fig. 1*A*). We then simulated the EPSP, IPSP, and the summed response at the soma (Fig. 2*A*), and defined SC in the same manner as that for experimental measurements. The dependence of SC on the amplitudes of EPSP (0.2–8 mV) and IPSP (0.1–3.5 mV) was plotted for *E* at 151 μm and for

NEUROSCIENCE

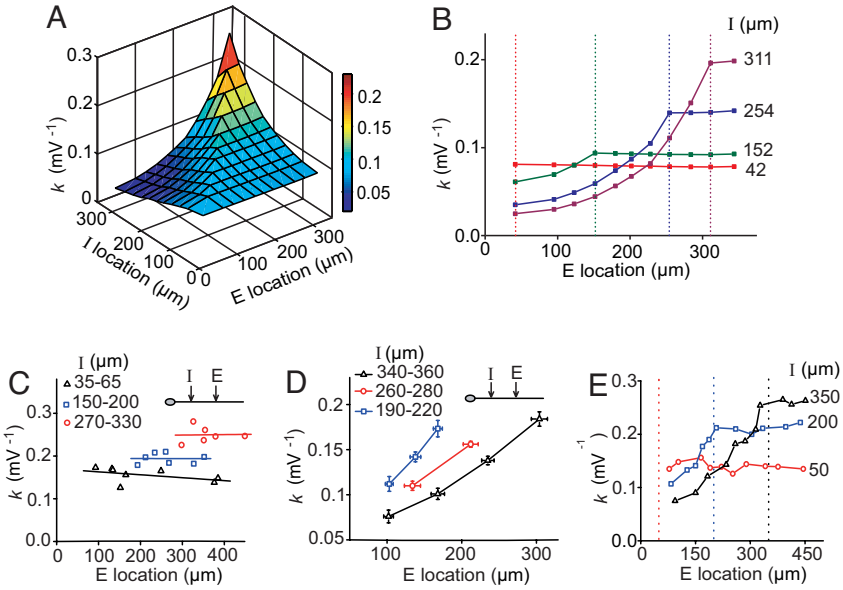

Fig. 3. Dependence of *k* on *E/I* locations. (*A* and *B*) Stimulation results showing coefficient *k* as a function of *E* and *I* distances from the soma. For each *E/I* location, *k* was computed from 20 sets of EPSP and IPSP amplitudes using the least-square fit. The value of *k* is color-coded (see bar) in a 3D map in *A*. In *B*, *k* is plotted as a function of *E* location, corresponding to the cross-section of the 3D map. Data points connected by each line depict *k* for a given *I* location (marked by the dashed line of the same color). (*C–E*) Experimental results on the location dependence of *k*. In *C*, changes of *k* with more distal *E* locations. Data grouped by the range of *I* locations. Line indicates best linear fit of each group. In *D*, changes of *k* with *E/I* locations of paired *E* and *I* from experiments in which *E* was more proximal to *I*, for different ranges of *I* location. Each point was averaged from more than three cells. In *E*, changes of *k* with *E* location, for three fixed *I* locations (marked by dashed lines).

I at 94 μm from the soma. Consistent with our experimental observations (Fig. 1 *E* and *F*), the SC amplitude depended linearly on both the EPSP and IPSP amplitudes (Fig. 2*B* and Fig. S3*B*).

Besides the above studies using fixed EPSP or IPSP amplitude, we further characterized the dependence of SC on IPSP and EPSP amplitudes by randomly varying both the EPSP (in a range of 0.2 to 10 mV) and the IPSP (0.1–4 mV) in experiments and simulations. When the amplitude ratio SC/EPSP was plotted against the IPSP amplitude or when SC/IPSP was plotted against the EPSP amplitude, we found that these two plots could be well fitted by straight lines through the origin, with nearly identical slopes (Fig. 2 *C* and *D*). This finding suggests that SC is directly proportional to EPSP*IPSP. We also plotted the simulated SC amplitude against both EPSP and IPSP amplitudes (Fig. 2*E*) and fitted the results by the function SC = *k**EPSP*IPSP, with *k* as the free parameter (Fig. 2*F*). This multiplicative function provided a good approximation (rms error: 4.9%) for simulated SC over a range of EPSP and IPSP amplitudes. Thus, the summed response to coincident *E* and *I* can be approximated by a simple arithmetic rule:

$$Sum = EPSP + IPSP + k^* EPSP^* IPSP, \qquad [1]$$

where *k* (in the unit of mV^{-1}) reflects the strength of shunting inhibition ($k > 0$ for hyperpolarizing IPSPs). This arithmetic rule quantitatively describes two aspects of inhibition: hyperpolarization and shunting inhibition.

Dependence of *k* on *E* and *I* Locations Along the Apical Dendritic Trunk. We further examined the dependence of *k* on *E* and *I* locations along the apical dendrite trunk in the CA1 pyramidal neuron model. For each combination of *E* and *I* locations, we computed the *k* value from 20 sets of arbitrarily chosen *E* and *I* amplitudes and plotted the results in Fig. 3*A*. As shown by the various cross-sections of the 3D graph, for each *I* location the dependence of *k* on the *E* location showed a clear asymmetry for proximal vs. distal *E*s (Fig. 3*B*): For a given *I*, the *k* value decayed rapidly with the *I–E* distance for proximal *E*s (space constant ≈83 μm), but remained relatively constant for distal *E*s. The maximal *k* value was higher for more distal *I*s.

The dependence of *k* on *E* and *I* locations observed in the above simulations was also tested experimentally by iontophoresis of glutamate and GABA at various locations along the main dendritic trunk of the CA1 pyramidal cell. For *E* at more distal sites than *I* (at three sets of *I* locations), *k* was largely independent of the *E* location and *E–I* distance, but markedly dependent on the *I* location (Fig. 3*C*). For *E*s located proximally to *I* (at three sets of *I* locations), *k* decreased with the *E–I* distance (Fig. 3*D*), consistent with that found by simulation. Finally, when *k* was plotted as a function of the *E* location for various fixed *I* locations, the *k* profile also showed a clear distal-proximal asymmetry (Fig. 3*E*), similar to that found by simulation. These results support and extend the notion of on-the-path shunting (10, 11).

Shunting Inhibition Involving Oblique Branches. Because most synaptic inputs to pyramidal neurons are located on dendritic branches, we examined the shunting of *E*s distributed throughout the dendritic tree exerted by *I* located at either the dendritic trunk or an oblique branch. For each *I* location of the realistic neuronal model, we computed *k* as a function of the *E* location over the entire apical dendrite except at the distal *stratum lacunosum moleculare* layer, where local subthreshold EPSPs and IPSPs cause little change of the somatic membrane potential (16). For *I* located at the apical trunk (Fig. 4*A*), there was a prominent asymmetry; *k* values were uniformly large for distal *E*s at both the trunk and branches but decreased rapidly with the *E–I* distance for proximal *E*s. For *I* located at an oblique branch (Fig. 4*B*), shunting was largely confined to the same branch. This finding is in line with the idea that each dendritic branch is an independent functional compartment (4–5, 11, 17–22). Notably, the asymmetry in the *k* profile observed at the apical trunk (Fig. 3) was also observed at the oblique branch when *E* and *I* were located at the same branch; *k* was uniformly high for distal *E*s and decreased with the *E–I* distance for proximal *E*s (Fig. 4*B*).

The above modeling results were then tested experimentally in hippocampal slices. For the same location of GABA iontophoresis at an oblique branch, we measured the SC and calculated *k* for EPSPs induced at two locations along the same oblique branch. No significant difference was found in the *k* value ($P = 0.89$, paired *t* test) when the two *E* locations were both distal (spaced by ≈70 μm; Fig. 4*C*). In contrast, for two *E*s at more proximal locations, *k* was significantly smaller ($P = 0.001$) for the *E* closer to the branch point (Fig. 4*D*). Furthermore, for *I* located at the apical trunk, the *k* values were not significantly different for distal *E*s located at either the trunk or branch (Fig. 4*E*; $P = 0.92$, paired *t* test), consistent with the simulation results (Fig. 4*A*). When the *I*-soma distance was kept within 100–200 μm, *k* values for *I* and *E* located at the same branch were significantly higher than those for *I* and *E* located at different

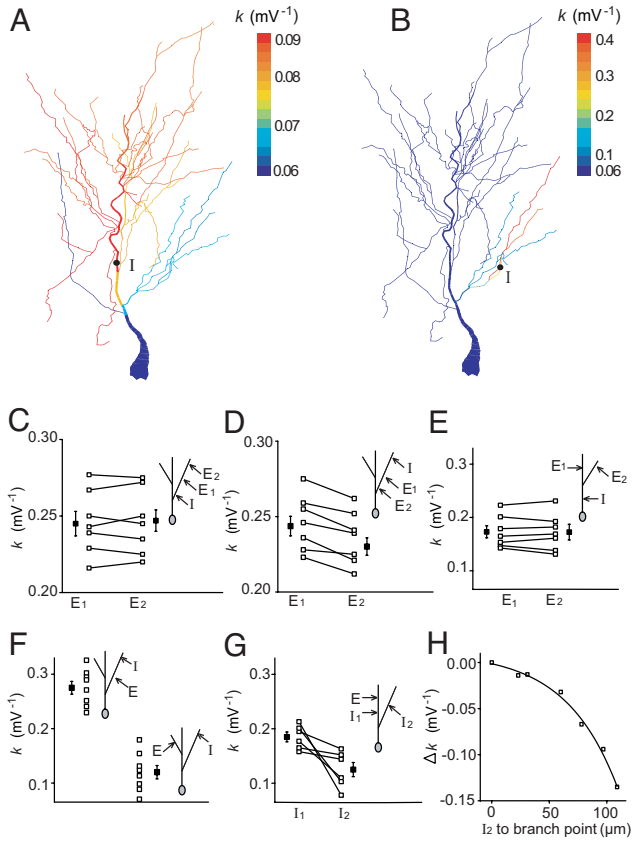

Fig. 4. Shunting inhibition for *I* located at dendritic trunk and oblique branches. (*A* and *B*) Simulation results of *k* values (color-coded) for *I* (black dot) located at apical trunk (*A*) and oblique branch (*B*), with *E* scattered on dendritic arbor in *stratum radiatum*. (*C*–*H*) Experimental results. (*C*) *I* at oblique branch: *k* was not significantly different between two distal *E*s (E_1 and E_2) within the same branch ($P = 0.89$, paired *t* test). E_1 to E_2 distances were >70 μm in all experiments. Lines connect data from the same cell. (*D*) As in *C* except that *E*s were more proximal to *I* ($P = 0.001$). (*E*) *I* at the trunk: *k* was not significantly different between *E*s at the trunk (E_1) and at the first-order oblique branch (E_2, $P = 0.92$). *I* to *E* distances were kept constant. (*F*) *I* at oblique branch: *k* was significantly different between *E*s at the same and different branch ($P < 0.001$). (*G*) *E* at the trunk: *k* was significantly different between *I*s at the trunk (I_1) and at oblique branch (I_2, $P = 0.031$). The trajectory distance of *I* to the soma was kept constant. (*H*) The decay of *k* value as a function of distance between I_2 and the branch point for the configuration in *G*. Line indicates exponential fit ($R = 0.97$, length constant 44 μm).

branches (Fig. 4*F*; $P < 0.001$). Finally, for a fixed *E* location at the apical trunk, the *k* values for more proximal *I*s at the branch were lower than those at the trunk (Fig. 4*G*; $P = 0.03$), with *k* decreasing rapidly with the distance to the branch point (Fig. 4*H*). Together, these experimental results are consistent with those found by simulation, indicating that shunting inhibition is largely compartmentalized to the same branch, with the distal–proximal asymmetry similar to that at the trunk.

Effects of Active Conductances and Transmitter Receptors. Previous studies of *E*–*I* integration mostly addressed the role of passive cable properties (1, 10, 11). We have examined systematically how different ion channels and transmitter receptors affect the extent of shunting inhibition. For the CA1 pyramidal cell model, we calculated the *k* values for 15 sets of randomly chosen *E* and *I* locations before and after blocking 90% of each of the following conductances: voltage-dependent Na^+ channel, delayed rectifier K^+ channel (K_d), A-type K^+ channel (K_A), hyperpolarization-activated cationic current (I_h), NMDA receptor (NMDAR), and $GABA_BR$ (see *SI Appendix*). As shown in Fig. 5*A*, 90% blockade of I_h, K_A,

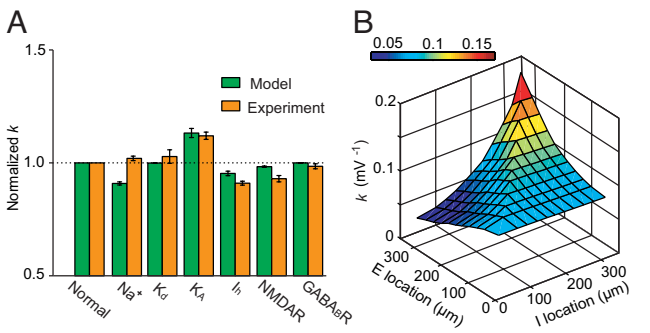

Fig. 5. Effects of ion channels and transmitter receptors on shunting inhibition. (*A*) Simulation (green) and experimental (orange) results on the changes in *k* after blockade of each of the ion channels and transmitter receptors. (*B*) 3D plot of *k* as a function of *E* and *I* locations after simultaneous blockade of voltage-dependent sodium conductance, delayed rectifier potassium conductance (K_d), A-type potassium conductance (K_A), I_h channel conductance, NMDARs, and $GABA_BRs$.

NMDAR, and Na^+ channels resulted in significant changes in the *k* value, whereas blockade of K_d and $GABA_BR$ had no effect. These simulation results were tested by iontophoretic experiments in hippocampal slices using *I* and *E* located at the apical trunk within 100–200 and 100–300 μm from the soma, respectively. Specific blockers of Na^+ channel (tetrodotoxin, 3 μM), K_d (tetraethylammonium, 3 mM), K_A (4-AP, 1 mM), I_h (ZD7288, 20 μM), NMDAR (D-AP5, 50 μM), and $GABA_BR$ (CGP35348, 60 μM) were used separately to block each of these channels or receptors. We found that K_A channel blockade increased the *k* value (≈12%, $P < 0.01$), an effect that may diminish the EPSP amplitude increase caused by the blockade of K_A channels (23). In contrast, blocking I_h and NMDARs decreased the *k* value by 9% and 7%, respectively ($P < 0.01$), indicating contributions of these channels to the shunting effect. However, blockade of K_d, Na^+ channels, and $GABA_BRs$ had no effect ($P > 0.4$; Fig. 5*A*). With the exception of the Na^+ channel, these experimental findings largely agreed with the simulation results. The discrepancy on Na^+ channel blockade may be attributed to a lower voltage threshold for the activation of Na^+ channels in the model cell.

We also examined the role of these ion channels and receptors in the dendrite-location dependence of *k* in the model. By comparing the *k* profile before and after 90% blockade of each of K_d, Na^+, K_A, I_h, NMDAR, and $GABA_BR$ channels, we found that although the overall *k* values were altered to different extents, the asymmetric spatial profile remained the same (Fig. S4). Furthermore, this asymmetry was found even after all of the above conductances and receptors were blocked (Fig. 5*B*). Thus, the asymmetry in the *k* profile results primarily from passive cable properties of the dendrite.

Theoretical Interpretation of the Arithmetic Rule. The theoretical basis of the arithmetic rule was next examined, using two-port analysis of the passive dendritic tree (ref. 11 and see *SI Appendix* and Fig. S5 for details). The analysis yielded a simple analytic expression for *E*–*I* summation:

$$V_s \approx V_{se} + V_{si} - K_{ei}\left(\frac{1}{K_{es}E_{ri}} + \frac{1}{K_{is}E_{re}}\right)V_{se}V_{si}, \qquad [2]$$

where V_s is the somatic voltage response to concurrent *E* and *I*, and V_{se} and V_{si} are the somatic response to the individual excitatory input at location *e* and to the individual inhibitory input at location *i*, respectively. K_{ei} is the transfer resistance between location *e* and *i*, K_{es} is between *e* and soma, and K_{is} is between *i* and soma. E_{re} and E_{ri} are the driving forces (the difference between the reversal

NEUROSCIENCE

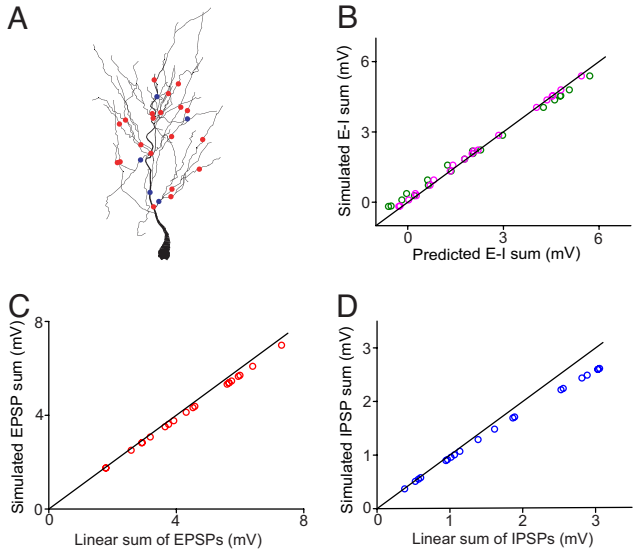

Fig. 6. Integration of multiple *E*s and *I*s. (*A*) Distribution of 20 *E*s (red dots) and 5 *I*s (blue dots) at the dendritic arbor of the model neuron. (*B*) Comparison between the simulated response and the responses predicted by Eqs. **4** (green) and **5** (magenta). (*C*) Summation of the 20 coactivated *E*s with individual conductances ranging from 0.05 to 0.48 nS. (*D*) Summation of the five *I*s with individual conductances ranging from 0.32 to 6.40 nS.

potential and resting membrane potential) for E and I, respectively. By defining

$$k = -K_{ei}\left(\frac{1}{K_{es}E_{ri}} + \frac{1}{K_{is}E_{re}}\right),$$

we obtain $V_s \approx V_{se} + V_{si} + kV_{se}V_{si}$.

This equation has the same form as the empirically derived arithmetic rule, for which V_s, V_{se}, and V_{si} correspond to sum, EPSP, and IPSP, respectively. Considering that $E_{ri} \ll E_{re}$, and K_{es} and K_{is} are of the same order of magnitude, k is reduced to

$$k \approx \frac{K_{ei}}{K_{es}(-E_{ri})}. \qquad [3]$$

Note that in the above equation, k is inversely proportional to E_{ri}, a relation confirmed in our simulation (Fig. S6). When E_{ri} approaches zero, k approaches infinity, but the product (k*IPSP) remains finite because IPSP also approaches zero. When E_{ri} becomes positive, as the case of early developing synapse (24), k should be negative, so that the shunting component (k*EPSP*IPSP) remains negative (Fig. S7).

Integration of Multiple *E*s and *I*s. Each CA1 pyramidal neuron receives a large number of inputs at its dendrite. Is the rule obtained from a pair of E and I applicable to multiple *E*s and *I*s? To address this question, we selected 20 *E*s and 5 *I*s randomly distributed in the dendritic tree of the model CA1 pyramidal cell (Fig. 6*A*), with a range of synaptic conductances (*E*s: 0.048–0.48 nS; *I*s: 0.32–6.4 nS). We first compared the simulated response to coincident activation of these *E*s and *I*s with that predicted by a simple arithmetic rule, in which the response was given by the linear sum of individual EPSPs and IPSPs together with all of the pairwise E–I interactions, using the following equation

$$Sum = \sum_i EPSP_i + \sum_j IPSP_j + \sum_{i,j} k_{ij} * EPSP_i * IPSP_j, \qquad [4]$$

where $EPSP_i$ and $IPSP_j$ are somatic responses evoked by E_i and I_j, respectively, and k_{ij} is a coefficient for the paired E_i and I_j (which depends on the dendritic locations of E and I but not on the amplitude or the number of other coactivated inputs). As shown in Fig. 6*B* (green circles), for 20 different sets of EPSP and IPSP amplitudes, the predicted responses deviated from the simulated responses (rms error was 8.5%) at both small and large sum amplitudes. This deviation could originate from nonlinear E–E and I–I interactions (2, 25), as indeed suggested by the systematic deviation of the simulated responses to 20 coincident *E*s (Fig. 6*C*) and 5 coincident *I*s (Fig. 6*D*) from the linear sum. We thus adjusted Eq. **4** by incorporating the nonlinear E–E and I–I interactions:

$$Sum = EPSP^S + IPSP^S + \sum_{i,j} k_{ij} * EPSP_i * IPSP_j, \qquad [5]$$

where $EPSP^S$ and $IPSP^S$ represent simulated somatic responses to coincident *E*s and *I*s alone, respectively. Eq. **5** yielded predicted responses in excellent agreement with simulated responses (Fig. 6*B*, magenta circles; rms error was 2.7%). Thus, the arithmetic rule for the pairwise E–I interaction can also be used for quantitative estimate of E–I integration with multiple coincident *E*s and *I*s. Of course, a complete arithmetic rule for multiple inputs can be obtained only if the rules for the summation of multiple EPSPs and multiple IPSPs are both available. Our finding on the E–I interaction represents an important step toward the goal of obtaining a complete rule for integration of multiple *E*s and *I*s.

Another potential consequence of simultaneous activation of a large number of inputs is the generation of somatic and/or dendritic spikes. We have tested whether the rule is valid in the presense of backpropagating action potentials (APs). In the simulation, an AP was evoked by injecting a depolarizing current (2 ms, 1.5 nA) into the soma, and the concurrent EPSP and IPSP were initiated 2, 5, or 10 ms after the AP. We then computed EPSP, IPSP, and the sum by subtracting the AP measured separately (Fig. S8*A*). We found that the arithmetic rule for subthreshold EPSP–IPSP summation still holds in the presence of a preceding AP (Fig. S8*B*). However, with the AP, there was an increase in the k value, which may be caused by the decrease of driving force for inhibitory input when the summation occurred at the after-hyperpolarization phase of AP (Fig. S8*A*). We also examined the interaction between an IPSP and a dendritic spike, which appeared as spikelet-EPSP at the soma (Fig. S9*A Inset*). In 46 of 79 dendrites tested, large excitatory inputs evoked somatic spikelets (the remaining 33 dendrites, in which dendritic spikes caused somatic APs, were excluded from the analysis). Among these 46 dendritic branches, the arithmatic rule holds for E (spikelet-EPSP) and I at different branches or for I at the trunk (Fig. S9 *A* and *B*), but it does not hold for E and I within the same branch (Fig. S9 *C* and *D*). This difference may be attributed to the mechanism for dendritic spike generation. When E and I are located at different dendritic branches, I had little impact on dendritic spike generation. However, the large shunting effect of I on the same branch can prevent or reduce dendritic spike generation induced by E, resulting in the violation of the simple arithmetic rule.

Discussion

Based on realistic neuronal modeling and experimental measurements, we derived a simple arithmetic rule that quantitatively describes the spatial summation of a pair of E and I at the apical dendrite of the CA1 pyramidal cell. The summed response at the soma is equal to the algebraic sum of EPSP, IPSP, and a nonlinear term proportional to the amplitudes of both EPSP and IPSP. The dependence of k on E/I locations revealed that for a given I shunting inhibition is similarly effective for all distal *E*s, but the effect on proximal *E*s falls off rapidly with the E–I distance. Moreover, for I at an oblique dendritic branch, the shunting effect is restricted mainly within the branch, with the same proximal/distal asymmetry.

Further studies showed that the asymmetry is determined largely by the passive cable properties and the empirically obtained arithmetic rule could be derived analytically from passive cable properties of the dendrite. Finally, we showed that this simple rule may also be applied to the integration of multiple *E*s and *I*s and under some circumstances in the presence of somatic or dendritic spikes, thus serving as a useful tool for studying *E–I* integration.

Nonlinear *E–I* integration caused by shunting of excitatory synaptic currents through activated $GABA_A$ channels has been shown experimentally (9, 26) and theoretically (8, 10, 11). Shunting inhibition was generally considered to be a divisive effect (8, 9). Here, the derivation of the simple arithmetic rule led to the identification of the coefficient *k* as a single parameter for describing the dependence of the shunting effect on *E* and *I* locations. Although there were some quantitative differences in the *k* values between simulations and experiments, the asymmetry in the *k* profile was similar. The smaller *k* values found by simulation could be attributed to the limitation of the dendrite model based on the cable equation (27) and the limited set of ion channels used in the simulation. Previous theoretical analysis based on passive cable properties has shown that shunting inhibition is maximally effective when *I* is between *E* and the soma (on-the-path effect; see refs. 10 and 11). Contradictory to this prediction, a study in cultured hippocampal neurons showed that nonlinear *E–I* interaction decreases rapidly with the *E–I* distance, regardless of whether *E* was located proximal or distal to *I* within the dendritic branch (12). Our finding of the asymmetric dendritic profile of *k* for both the apical trunk and oblique branches supports the on-the-path theory. The discrepancy between our results in hippocampal slices and those in culture may be mainly attributed to differences in the cable property. Moreover, we found that when *I* is located at an oblique branch, the shunting interaction is largely confined within the branch, similar to that found previously for both *E–E* (5, 6, 25) and *E–I* (12, 28) summation, supporting the view that each dendritic branch can serve as an independent computing compartment (4–5, 11, 17–22). Dendritic spikes are known to be involved in *E–E* summation within branches (3, 5, 6). Here, we found that the magnitude of *k* for *E–I* summation within the branch is much larger than the magnitude of *k* for *I*s at the trunk (Fig. 4 *A* and *B*). Thus, although *E–E* summation within the branch is more likely to evoke dendritic spikes, the potent shunting inhibition within branches may effectively regulate dendritic spike generation. The local vs. global effect of the branch- vs. trunk-located *I* endows the neuron with the flexibility for selective inhibitory control of *E*s distributed over the dendritic arbor.

Various types of inhibitory interneurons selectively innervate different dendritic domains of pyramidal cells (13, 14). For example, in the hippocampal CA1 region, O-LM cells and bistratified cells innervate the distal apical dendrite and the oblique branches, respectively, whereas basket cells selectively synapse onto the peri-somatic region (13, 29–31). Our results provide a quantitative basis for analyzing domain-specific inhibition by different interneurons. Most neural network models consist of point neurons (32–35) with no dendritic arbor, and synaptic inputs were often summed linearly to determine neuronal spiking. However, recent studies have highlighted the importance of dendritic morphology (19, 21, 22, 36) and nonlinear interactions (3, 4, 10, 11, 37) in neuronal computation. Our simple arithmetic rule offers an efficient tool for incorporating location specific *E–I* interactions into neural network models, to understand the role of various types of GABAergic interneurons in shaping network activity.

Materials and Methods

The procedure of electrophysiology recording in rat hippocampal slices followed that described (38). Computer simulation was performed by using the NEURON simulation environment. The details of iontophoresis and electrophysiological measurements, methods for the construction of the CA1 pyramidal neuron model and the simulation of *E–I* integration are described in *SI Appendix*. For statistical analysis, data are presented as mean ± SEM, unless otherwise noted, and Student's *t* test was used to determine the significance of the difference between results obtained from different experimental conditions.

ACKNOWLEDGMENTS. We thank B. Mel for helpful comments on the manuscript. This work was supported by Major State Basic Research Program of China Grant 2006CB806600. M.-m. P. and Y.D. were supported in part by grants from the National Institutes of Health.

1. Rall W (1964) in *Neural Theory and Modeling*, ed Reiss R (Stanford Univ Press, Stanford, CA), pp 73–97.
2. Cash S, Yuste R (1999) Linear summation of excitatory inputs by CA1 pyramidal neurons. *Neuron* 22:383–394.
3. Poirazi P, Brannon T, Mel BW (2003) Arithmetic of subthreshold synaptic summation in a model CA1 pyramidal cell. *Neuron* 37:977–987.
4. Poirazi P, Brannon T, Mel BW (2003b) Pyramidal neuron as two-layer neural network. *Neuron* 37:989–999.
5. Polsky A, Mel BW, Schiller J (2004) Computational subunits in thin dendrites of pyramidal cells. *Nat Neurosci* 7:621–627.
6. Losonczy A, Magee JC (2006) Integrative properties of radial oblique dendrites in hippocampal CA1 pyramidal neurons. *Neuron* 50:291–307.
7. Eccles J (1961) The nature of cortical inhibition. *Proc R Soc London Ser B* 445–476.
8. Blomfield S (1974) Arithmetical operations performed by nerve cells. *Brain Res* 69:115–124.
9. Fatt P, Katz B (1953) The effect of inhibitory nerve impulses on a crustacean muscle fiber. *J Physiol (London)* 121:374–389.
10. Koch C, ed (1999) *Biophysics of Computation* (Oxford Univ Press, New York).
11. Koch C, Poggio T, Torre V (1983) Nonlinear interactions in a dendritic tree: Localization, timing, and role in information processing. *Proc Natl Acad Sci USA* 80:2799–2802.
12. Liu G (2004) Local structural balance and functional interaction of excitatory and inhibitory synapses in hippocampal dendrites. *Nat Neurosci* 7:373–379.
13. Somogyi P, Klausberger T (2005) Defined types of cortical interneurone structure space and spike timing in the hippocampus. *J Physiol (London)* 562:9–26.
14. Somogyi P, Tamas G, Lujan R, Buhl EH (1998) Salient features of synaptic organization in the cerebral cortex. *Brain Res Brain Res Rev* 26:113–135.
15. Cannon RC, Turner DA, Pyapali GK, Wheal HV (1998) An online archive of reconstructed hippocampal neurons. *J Neurosci Methods* 84:49–54.
16. Jarsky T, Roxin A, Kath WL, Spruston N (2005) Conditional dendritic spike propagation following distal synaptic activation of hippocampal CA1 pyramidal neurons. *Nat Neurosci* 8:1667–1676.
17. Llinas R, Nicholson C (1971) Electrophysiological properties of dendrites and somata in alligator Purkinje cells. *J Neurophysiol* 34:532–551.
18. Koch C, Poggio T, Torre V (1982) Retinal ganglion cells: A functional interpretation of dendritic morphology. *Philos Trans R Soc London Ser B* 298:227–263.
19. Stuart G, Spruston N, Hausser M, eds (1999) *Dendrites* (Oxford Univ Press, Cary, NC).
20. Archie KA, Mel BW (2000) A model for intradendritic computation of binocular disparity. *Nat Neurosci* 3:54–63.
21. Segev I, London M (2000) Untangling dendrites with quantitative models. *Science* 290:744–750.
22. London M, Hausser M (2005) Dendritic computation. *Annu Rev Neurosci* 28:503–532.
23. Hoffman DA, Magee JC, Colbert CM, Johnston D (1997) K^+ channel regulation of signal propagation in dendrites of hippocampal pyramidal neurons. *Nature* 387:869–875.
24. Ben-Ari Y, Gaiarsa JL, Tyzio R, Khazipov R (2007) GABA: A pioneer transmitter that excites immature neurons and generates primitive oscillations. *Physiol Rev* 87:1215–1284.
25. Tamas G, Szabadics J, Somogyi P (2002) Cell type- and subcellular position-dependent summation of unitary postsynaptic potentials in neocortical neurons. *J Neurosci* 22:740–747.
26. Borg-Graham LJ, Monier C, Fregnac Y (1998) Visual input evokes transient and strong shunting inhibition in visual cortical neurons. *Nature* 393:369–373.
27. Qian N, Sejnowski TJ (1990) When is an inhibitory synapse effective? *Proc Natl Acad Sci USA* 87:8145–8149.
28. Skydsgaard M, Hounsgaard J (1994) Spatial integration of local transmitter responses in motoneurones of the turtle spinal cord in vitro. *J Physiol (London)* 479:233–246.
29. Freund TF, Buzsaki G (1996) Interneurons of the hippocampus. *Hippocampus* 6:347–470.
30. Parra P, Gulyas AI, Miles R (1998) How many subtypes of inhibitory cells in the hippocampus? *Neuron* 20:983–993.
31. Klausberger T, et al. (2004) Spike timing of dendrite-targeting bistratified cells during hippocampal network oscillations in vivo. *Nat Neurosci* 7:41–47.
32. McCulloch W, Pitts W (1943) A logical calculus of the ideas immanent in nervous activity. *Bull Math Biol* 5:115–133.
33. Rosenblatt F, ed (1962) *Principles of Neurodynamics* (Spartan Books, New York).
34. Hopfield J (1982) Neural networks and physical systems with emergent collective computational abilities. *Proc Natl Acad Sci USA* 79:2554–2558.
35. Maass W (1997) Networks of spiking neurons: The third generation of neural network models. *Neural Networks* 10:1659–1671.
36. Hausser M, Spruston N, Stuart G (2000) Diversity and dynamics of dendritic signaling. *Science* 290:739–744.
37. Mel BW (1993) Synaptic integration in an excitable dendritic tree. *J Neurophysiol* 70:1086–1101.
38. Xu C, Zhao M-X, Poo MM, Zhang XH (2008) $GABA_B$ receptor activation mediates frequency-dependent plasticity of developing GABAergic synapses. *Nat Neurosci* 11:1410–1418.